Acta Pharmaceutica Sinica B 2024;14(12):5370–5381

Chinese Pharmaceutical Association
Institute of Materia Medica, Chinese Academy of Medical Sciences

Acta Pharmaceutica Sinica B

www.elsevier.com/locate/apsb
www.sciencedirect.com

ORIGINAL ARTICLE

Pretheranostic agents with extraordinary NIRF/photoacoustic imaging performance and photothermal oncotherapy efficacy

Liu Shi [a,b,†], Zhenzhou Chen [a,c,†], Jiaxin Ou [a,†], En Liang [a], Zhipeng Chen [a], Qiuyue Fu [a], Lan Huang [a,*], Kui Cheng [a,b,*]

[a] *Guangdong Provincial Key Laboratory of New Drug Screening, NMPA Key Laboratory for Research and Evaluation of Drug Metabolism and Guangdong-Hong Kong-Macao Joint Laboratory for New Drug Screening, School of Pharmaceutical Sciences, Southern Medical University, Guangzhou 510515, China*
[b] *State Key Laboratory of Organ Failure Research, Key Laboratory of Infectious Diseases Research in South China, Ministry of Education, Southern Medical University, Guangzhou 510515, China*
[c] *Jieyang Medical Research Center, Jieyang People's Hospital, Jieyang 522000, China*

Received 6 April 2024; received in revised form 19 June 2024; accepted 16 July 2024

KEY WORDS

Biothiol detection;
Near-infrared fluorescence (NIRF) imaging;
Photoacoustic (PA) imaging;
Photothermal therapy (PTT);
Cervical cancer

Abstract Cervical cancer, the most common gynecological malignancy, significantly and adversely affects women's physical health and well-being. Traditional surgical interventions and chemotherapy, while potentially effective, often entail serious side effects that have led to an urgent need for novel therapeutic methods. Photothermal therapy (PTT) has emerged as a promising approach due to its ability to minimize damage to healthy tissue. Connecting a biothiol detection group to PTT-sensitive molecules can improve tumor targeting and further minimize potential side effects. In this study, we developed a near-infrared fluorescence (NIRF)/photoacoustic (PA) dual-mode probe, S-NBD, which demonstrated robust PTT performance. This innovative probe is capable of activating NIRF/PA signals to enable the detection of biothiols with high emission wavelength (838 nm) and large Stokes shift (178 nm), allowing for *in vivo* monitoring of cancer cells. Additionally, the probe achieved an outstanding photothermal conversion efficiency of 67.1%. The application of laser irradiation (660 nm, 1.0 W/cm^2, 5 min) was able to achieve complete tumor ablation without recurrence. In summary, this seminal study presents a pioneering NIRF/PA dual-mode dicyanoisophorone-based probe for biothiol imaging, incorporating features from PTT for the first time. This pioneering approach achieves the dual objectives of improving tumor diagnosis and treatment.

*Corresponding authors.
E-mail addresses: huanglanmidea@163.com (Lan Huang), chengk@smu.edu.cn (Kui Cheng).
[†]These authors made equal contributions to this work.
Peer review under the responsibility of Chinese Pharmaceutical Association and Institute of Materia Medica, Chinese Academy of Medical Sciences.

https://doi.org/10.1016/j.apsb.2024.07.017

1. Introduction

Cysteine (Cys), homocysteine (Hcy), glutathione (GSH), and hydrogen sulfide (H_2S), the four primary small-molecule biothiols, play important roles in mediating critical physiological and pathological processes within the biological system[1-6]. However, the concentration of thiols is also closely associated with several diseases. Abnormal levels of Cys have been linked to growth retardation, neurotoxicity, liver damage, and white blood cell loss[7], while Hcy has been shown to increase the risk of neurovascular disease, diabetes, developmental disorders, and epilepsy[8]. GSH, the most abundant biothiol in cells, is essential for maintaining redox homeostasis but is also related to cancer, metabolic disorders, heart disease, and liver damage[9,10]. H_2S, an important endogenous gas signal transduction medium, is involved in cell signal transduction and anti-oxidation and impacts many immune regulatory processes within the body[11,12]. Given the important role biothiols play in the body, the design and production of molecular probes capable of monitoring their levels *in vivo* are crucial for diagnosing biothiol-related diseases. Cervical cancer in particular is characterized by the overexpression of biothiols, with a substantial upregulation of biothiol levels observed in human cervical cancer cells and tumors[13].

Near-infrared fluorescence (NIRF) imaging offers unique advantages for detection and diagnosis, including high specificity and sensitivity[14-17]. However, the spatial resolution of optical imaging is significantly diminished as tissue depth increases, the result of light scattering effects. Consequently, the imaging capability is limited and only allows for the observation of superficial tumors[18,19]. Recently, photoacoustic imaging has emerged with *in vivo* capabilities extending up to a range of a few centimeters, offering better permeability and higher imaging resolution for deep tissues[20,21]. Hence, the combination of fluorescence and photoacoustic imaging, referred to as dual-modal imaging, has the potential to capitalize on the advantages of each method and is expected to enhance the effectiveness and reliability of tracking deep *in vivo* analytes[22,23].

Photothermal therapy (PTT) approaches used in recent years are still highly regarded as non-invasive treatment methods[24-28]. In PTT, photoresponsive probes actively or passively gather at the tumor site, converting light energy into heat energy by absorbing near-infrared lasers to irreversibly destroy cancer cells in the tumor tissue[29,30]. PTT offers several advantages over traditional cancer treatment methods, including less damage to healthy tissues, a minimally invasive procedure, higher ablation efficiency, shorter treatment duration, and tangible therapeutic effects[31,32].

To achieve NIRF/PA dual-modal detection while preserving the PTT effect, we designed a "three-in-one" probe (S-NBD). Our group had previously reported several compound molecules with excellent performance after structural modification[33-37]. In this study, we expanded the capabilities of the original probe by introducing diphenylamine and NBD structures[38,39], endowing it with photothermal properties that can detect and distinguish biothiols by NIRF/PA Imaging. The updated probe consists of three key components: heteroanthracene, which comprises the core nucleus structure, and functions as an electron-donating element providing excess electrons (D); dicyanoisophorone, which acts as the electron acceptor portion (A); and alkene bond, which serves as a π conjugate, linking the donor and acceptor, extending the conjugation length of the compound, and resulting in a longer emission wavelength as well as a larger Stokes shift. The rigid planar structures and strong interactions between chromophores in the D−π−A structure enhance non-radiative decay, thereby improving photothermal efficiency[40]. Meanwhile, diphenylamine was introduced onto the oxanthracene ring to construct a triphenylamine-like structure with stable free radical properties. The dihedral angle of the three benzene rings connected by N atoms gradually increased, which is beneficial for enhancing the ICT effect, reducing the energy gap between singlet and triplet states (DEST), and leading to enhanced non-radiative transitions in photoacoustic and photothermal properties[41-44]. In addition, the embedded NBD structure serves as a recognition site for biothiols. Substitution reactions occur in the presence of these biothiols, releasing near-infrared fluorescent groups and leading to the enhancement of NIRF signals and PA signals. Meanwhile, NBD rearranges after binding to Cys/Hcy, and fluorescence can be generated by 470 nm laser excitation, thus distinguishing Cys/Hcy from GSH/NaHS (Fig. 1).

In this study, we propose a dual-mode probe that overcomes the limitations of single NIRF probes to achieve superior optical imaging capabilities. As will be seen, this probe demonstrated remarkable photothermal performance, allowing for the temperature of tumor sites to be increased locally and achieving the effect of tumor thermal ablation. For the first time, a probe has been designed to detect biothiols *via* NIRF/PA dual-modal imaging while concurrently possessing photothermal properties for *in vivo* cervical cancer treatment.

2. Results and discussion

2.1. Probe design and chemical synthesis

We synthesized the probe S-NBD from cyclohexanone through 7 steps including Vilsmeier Haack reaction, cycloaddition, coupling, demethylation, condensation, and substitution. The synthetic route is described in Scheme 1, with the compounds synthesized in accordance with prior research[45,46]. Detailed synthesis information for each compound can be found in the Supporting Information The ^{1}H-NMR, ^{13}C-NMR, and mass spectra details are shown in Supporting Information Figs. S1−S20.

2.2. Fluorescent detection for biothiols in vitro

Firstly, UV spectroscopy (Fig. 2A) was employed to assess the sensing behavior of S-NBD for Cys, Hcy, GSH, and NaHS. Following the addition of Cys, Hcy, GSH, and NaHS, a slight redshift and enhancement of the original absorption peak were observed. Specifically, in reaction to Cys/Hcy, a new absorption

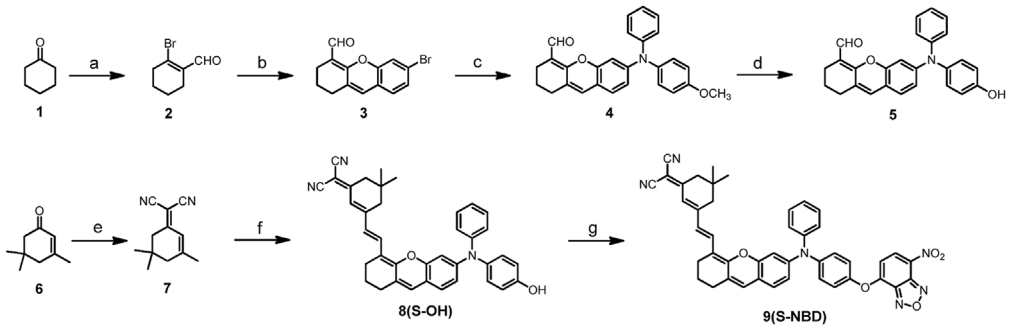

Scheme 1 Synthetic route to S-NBD. (a) PBr_3, DMF, $CHCl_3$, 0 °C, 8 h, 61%; (b) 4-bromo-2-hydroxybenzaldehyde, Cs_2CO_3, DMF, 16 h, 42%; (c) 4-methoxy-*N*-phenylaniline, $Pd_2(dba)_3$, x-phos, Cs_2CO_3, N_2, 110 °C, 16 h, 58%; (d) BBr_3, DCM, 0 °C, 4 h, 94%; (e) malononitrile, piperidine, CH_3CN, 81 °C, 12 h, 74%; (f) Compound **5**, CH_3CN, N_2, 81 °C, 10 h, 36%; (g) 4-Chloro-7-nitrobenzo[*c*][1,2,5]oxadiazole, DCM, Et_3N, 0 °C, 2 h, 47%.

peak appeared at 470 nm. When reacting with glutathione, no new peaks appeared. The addition of NaHS led to a reaction with S-NBD, generating a new absorption peak at 565 nm. To optimize imaging conditions, fluorescence intensity was measured by exciting the probe with/without Hcy at 660 nm in different EtOH/PBS solution proportions. Supporting Information Fig. S21 shows the greatest fluorescence enhancement in EtOH/PBS (pH 7.4, *v*/*v*, 5/5).

Following a 30-min reaction between S-NBD and the biothiols (Cys, Hcy, GSH, and NaHS), emissions were observed by excitation at 660 nm (Fig. 2B). The results revealed a new emission peak at 838 nm, with fluorescence enhancement observed in solutions containing biological mercaptan, including Cys (55-fold), Hcy (43-fold), GSH (48-fold), and NaHS (54-fold). Conversely, the solution containing only the probe did not exhibit fluorescence enhancement. Notably, only the solutions containing Cys and Hcy exhibited significant fluorescence enhancement at 550 nm (excited at 470 nm), reaching 90- and 106-fold, respectively. However, when NaHS was added to the S-NBD solution and excited by 565 nm laser, no fluorescence enhancement was observed.

To investigate the temporal response of S-NBD to the biothiols (Cys, Hcy, GSH, and NaHS), the UV absorption spectra (Supporting Information Fig. S22) and fluorescence spectra (Supporting Information Fig. S23) of S-NBD mixed with biothiols were immediately obtained. The results demonstrated a gradual increase in S-NBD fluorescence intensity which reached a plateau at approximately 30 min (Fig. 2C and D). As the concentration of Cys, Hcy, GSH, and NaHS varied, changes in UV absorption were also observed, indicating that absorption increased as concentrations rose, as shown in Supporting Information Fig. S24.

Subsequent examination of fluorescence intensities within biothiol concentrations revealed a clear signal at 838 with 660 nm laser excitation (Supporting Information Fig. S25A−S25D). Increases in fluorescence intensity were linked to rises in biothiol concentrations (0−200 μmol/L). As shown in Fig. S25E−S25H, linear relationships (R^2 = 0.99399 for Cys, R^2 = 0.99306 for Hcy, R^2 = 0.99531 for GSH, and R^2 = 0.99258 for NaHS) with biothiol concentrations were identified in the range of 0.0−10.0 μmol/L. In addition, the calculated limit of detection (LOD) for 10.0 μmol/L S-NBD was determined to be 10.8, 27.9,

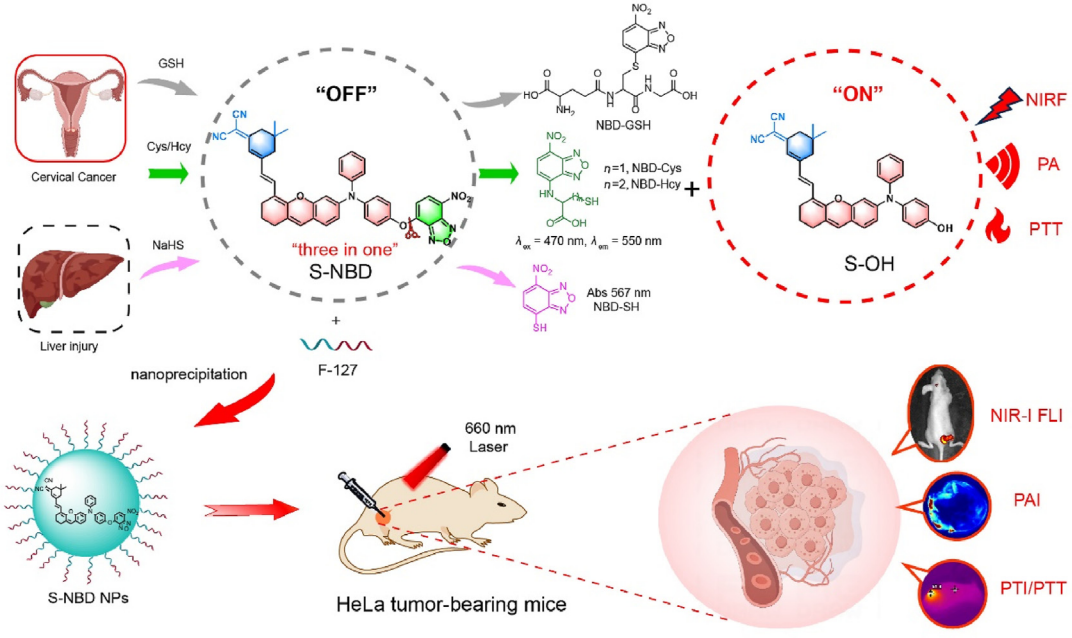

Figure 1 Schematic diagram of the dual-mode NIRF/PA S-NBD probe functions for biothiol detection and PTT in cervical cancer.

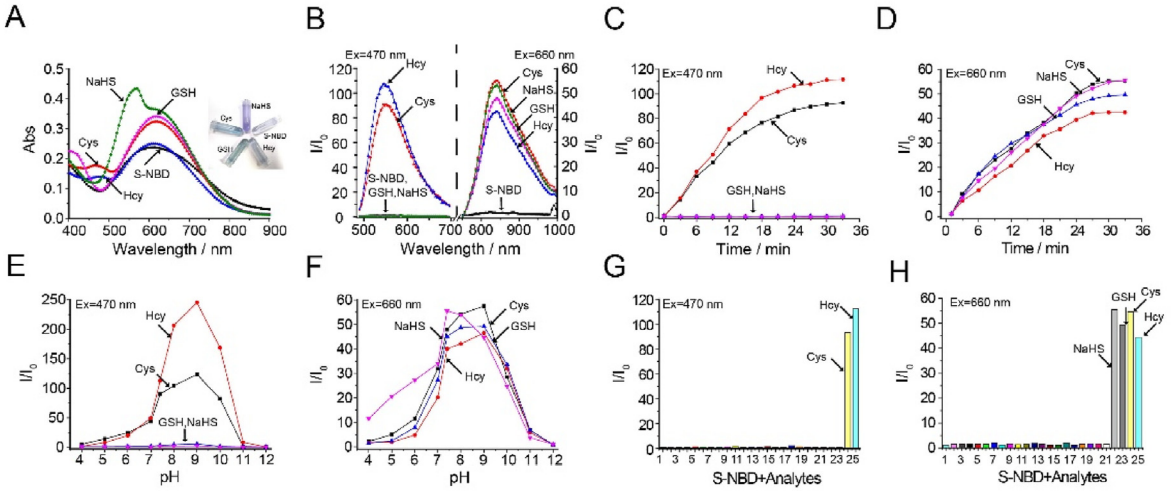

Figure 2 (A) Absorption spectra and (B) fluorescence spectra of S-NBD (10 μmol/L) in the presence of 10 equiv. of Cys/Hcy/GSH and NaHS in EtOH-PBS (pH 7.4, *v*/*v*, 5/5). Time-dependent fluorescence spectra of S-NBD (10 μmol/L) in the presence of 100 μmol/L of Cys/Hcy/GSH and NaHS (C) at 550 nm (λ_{ex} = 470 nm) and (D) at 838 nm (λ_{ex} = 660 nm). Fluorescence intensity of S-NBD (10 μmol/L) reacted with Cys/Hcy/GSH and NaHS (100 μmol/L) in different pH solutions. (E) at 550 nm (λ_{ex} = 470 nm) and (F) at 838 nm (λ_{ex} = 660 nm). Fluorescence intensity of S-NBD (10 μmol/L) reacted with various amino acids and metal ions (100 μmol/L) for 30 min, (G) λ_{ex} = 470 nm and (H) λ_{ex} = 660 nm (1, Blank; 2, Arg; 3, Gly; 4, Thr; 5, Gln; 6, Ala; 7, Try; 8, Leu; 9, Lys; 10, Phe; 11, Val; 12, Tyr; 13, Pro; 14, His; 15, Iso; 16, Glu; 17, Fe^{3+}; 18, Al^{3+}; 19, Mg^{2+}; 20, Cu^{2+}; 21, K^{+}; 22, NaHS; 23, GSH; 24, Cys; 25, Hcy).

20.1, and 23 nmol/L for Cys, Hcy, GSH, and NaHS, respectively, based on the fitting equations (Cys: $y = 1.31646 + 1.3481x$, Hcy: $1.24929 + 0.72703x$, GSH: $y = 0.81463 + 1.00427x$, NaHS: $y = 0.82045 + 0.81989x$). From Fig. S25I−J, it can be seen that upon the gradual addition of Cys/Hcy (0−200 μmol/L), an intense fluorescence signal at 550 nm appeared under the 470 nm excitation condition. This signal corresponds to that of NBD-Cys/Hcy. As biothiols were gradually added, a strong linear relationship (R^2 = 0.98741 for Cys and R^2 = 0.9857 for Hcy) was observed between the fluorescence intensity of NBD-Cys/Hcy and the biothiol concentration. Therefore, Cys/Hcy can be distinguished from GSH/NaHS through 470 nm laser excitation.

Additionally, we investigated the effect of solution pH on fluorescence intensity (Fig. 2E and F). S-NBD reactions with biothiols (Cys/Hcy and GSH) exhibited the highest fluorescence intensity enhancement at pH 9, while the probe detected NaHS exhibiting its highest fluorescence intensity enhancement at pH 7.4. For the selectivity test, 10 μmol/L S-NBD was incubated with various metal ions and amino acids (Arg; Gly; Thr; Gln; Ala; Try; Leu; Lys; Phe; Val; Tyr; Pro; His; Iso; Glu; Fe^{3+}; Al^{3+}; Mg^{2+}; Cu^{2+}; K^{+}; NaHS; GSH; Cys; Hcy) at 100 μmol/L for 30 min (Fig. 2G and H). The results showed that only biothiols (Cys, Hcy, GSH, and NaHS) resulted in significant fluorescence enhancement. In the presence of other analytes, the fluorescence remained unchanged, demonstrating the probe's excellent selectivity when detecting biothiols.

To verify the photo-stability of probe S-NBD, we conducted stability tests. Use a multifunctional enzyme-linked immunosorbent assay (ELISA) reader for testing, and start the detection when the probe interacts with Cys and the fluorescence reaches its maximum. Set the parameters to an excitation wavelength of 660 nm and an emission wavelength of 838 nm. After each fluorescence scan, oscillate for 10 s and wait for 10 s before starting a new round of scanning. The process lasted for 1 h, and the results are shown in the figure. The fluorescence of only the probe solution and the mixed solution of the probe and Cys remained constant. This experiment verified the stability of probe S-NBD towards light (Supporting Information Fig. S26).

Subsequently, we investigated the fluorescence imaging and photoacoustic imaging effects of probe S-NBD and probe nanoparticle S-NBD NPs. Taking Cys as an example, the fluorescence intensity changes of S-NBD and S-NBD NPs solutions were studied with the variation of Cys concentration. Meanwhile, the changes in fluorescence intensity of S-NBD and S-NBD NPs solutions with the addition of Cys over time were studied. As shown in Supporting Information Fig. S27, with the increase of Cys concentration, the fluorescence of the probe solution with/without nanoparticle encapsulation increases, and the fluorescence intensity of the nanoparticle probe for detecting Cys is slightly weaker than that of the probe without encapsulation. As shown in Supporting Information Fig. S28, after adding Cys, the fluorescence intensity of the nanoparticle probe reached its maximum and remained stable at about 33 min, slightly delayed compared to the uncoated probe. These phenomena may be caused by the slight influence of nanoparticles on the release of probes.

The theoretical reaction process is shown in Fig. 1. As can be seen, S-NBD itself does not exhibit fluorescence. After the probe undergoes a substitution reaction with biothiols, the fluorophore S−OH is released, which possesses both fluorescence and photoacoustic properties. Conversely, the second fluorophore NBD plays a crucial role in distinguishing Cys/Hcy from GSH/NaHS. When S-NBD undergoes a substitution reaction with NaHS, NBD-SH is generated, resulting in an increase in absorbance at 567 nm, thereby achieving the identification of NaHS. However, it was discovered that there was no fluorescence at the 567 nm excitation level. With regard to the Cys/Hcy reaction, rearrangement occurred after the substitution reaction, producing either NBD-Cys or NBD-Hcy with fluorescence in the green channel. As for the GSH reaction, the product NBD-GSH did not produce fluorescence in the NBD channel.

In order to further explore the reaction of the probe with biothiols, we performed theoretical DFT/TDDFT calculations. The

frontier molecular orbitals and the energy profiles for S-NBD and S−OH probes are shown in Fig. 3. In the ground state (S_0), the conjugation of S-NBD was poor, and the electron clouds of the LUMO and HOMO orbitals were relatively dispersed. In the excited state (S_1), no fluorescence phenomenon was observed due to the hindrance of the LUMO→HOMO electron transition (f = 0.0064). Following the addition of biothiols, S-NBD was converted into S−OH, the HOMO and LUMO of the S_0 and S_1 states were repositioned to the oxygen-containing anthracene moiety, and the electron clouds of the HOMO and LUMO orbitals overlapped, resulting in significant fluorescence signals from S−OH. The first vertical excitation energy (f = 1.0884, 839.15 nm) calculated was consistent with the experimental maximum emission wavelength, validating the reliability of the theoretical simulation results.

2.3. *Photoacoustic imaging for biothiols in vitro*

For photoacoustic imaging, strong NIR absorption was visible after S-NBD reacted with biothiols, indicating that S-NBD may elicit robust PA signals. The PA signals of the S-NBD probe in the absence or presence of Cys were subsequently measured in EtOH/PBS (pH 7.4, *v*/*v*, 5/5), revealing an optimal PA signal at 680 nm (Supporting Information Fig. S29). Once the optimal excitation wavelength was obtained, the effect of pH on PA signal strength was investigated in the presence of Cys, Hcy, GSH, and NaHS. The results showed that when S-NBD reacted with biothiols (Cys, Hcy, and GSH), S-NBD's PA intensity increased the most at pH 9, while the PA intensity of the probe for NaHS increased the most at pH 7.4 (Fig. 4A and B), aligning with the results of the fluorescence spectrum analysis. Next, the PA spectra for S-NBD with different concentrations of biothiols were examined, and the results revealed that when the concentration of biothiol increased, the PA strength increased as well (Fig. 4C and D). Therefore, the viewpoint espoused in this paper suggesting that the S-NBD probe has a specific response to biothiols *in vitro*, resulting in a significant enhancement of NIRF and PA, is confirmed. This discovery holds promise for the detection of biothiols at the cellular level in future applications.

In addition, we also studied the photoacoustic imaging of Cys using probes with/without nanocapsules. The results are shown in Supporting Information Fig. S30. As the concentration of Cys increases, the photoacoustic signal of the probe solution with/without nanocapsules increases, and the photoacoustic intensity of the nanoprobes detecting Cys is slightly weaker than that of the probes without nanocapsules. Consistent with the fluorescence analysis results.

During photothermal imaging of S-NBD *in vitro*, it was found that the precipitation of S-NBD occurred upon laser irradiation. To enhance biocompatibility, Pluronic F-127 and hydrophobic S-NBD were dissolved in THF and self-assembled into S-NBD NPs through the nanoprecipitation method. S-NBD NPs exhibited no precipitation following laser irradiation, effectively addressing the problem of poor water solubility of the compounds (Fig. 4E). Dynamic light scattering (DLS) experiments revealed that the nanoparticle size of S-NBD NPs is approximately 142 nm, with morphology and size elucidated by TEM (Fig. 4F). Interestingly, the size of the S-NBD NPs in PBS remained stable for 29 days, demonstrating the probe's stability (Supporting Information Fig. S31). Subsequently, the encapsulation efficiency and drug loading of the nanoparticles were investigated. The calculated encapsulation efficiency of the nanoparticles is 65.8%, and the drug loading rate is 4.8% (Supporting Information Fig. S32).

Inspired by the excellent PA response performance discussed above, we decided to further investigate the photothermal properties of S-NBD NPs. Firstly, S-NBD NPs and S−OH NPs (100 μmol/L) were laser irradiated at 660 nm (1 W/cm^2) for 10 min, and the temperature changes were recorded. The results showed comparable temperature changes for both types of NPs, and both exhibited excellent photothermal properties (Supporting Information Fig. S33). Next, we explored the relationship between the concentration of S-NBD NPs in PBS and temperature changes. As shown in Fig. 4G, when the concentration of S-NBD NPs reached 200 μmol/L, the solution temperature rapidly increased to 66.7 °C under NIR laser irradiation (660 nm, 1 W/cm^2, 10 min). It is worth noting that under the same conditions, S-NBD NPs with a relatively low concentration of 20 μmol/L still exhibited excellent photothermal performance, reaching a maximum temperature of

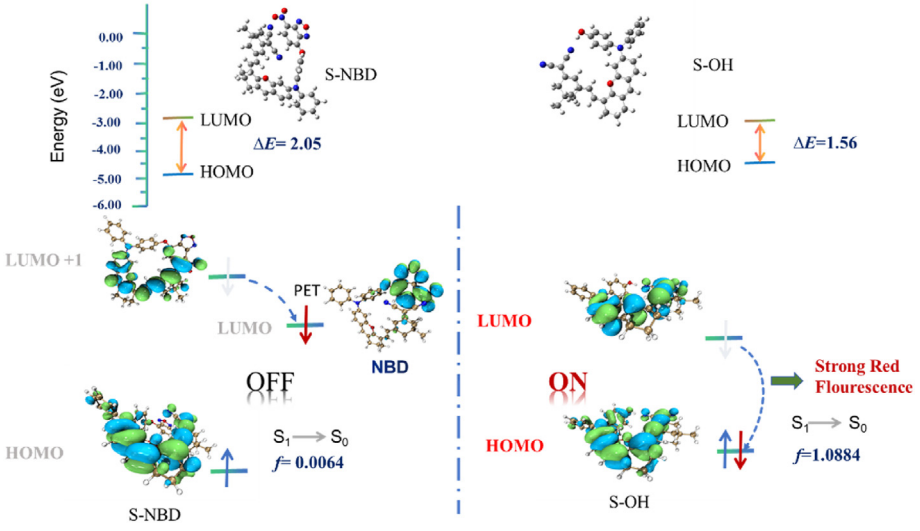

Figure 3 Frontline molecular orbital energy maps of probes S-NBD and S−OH.

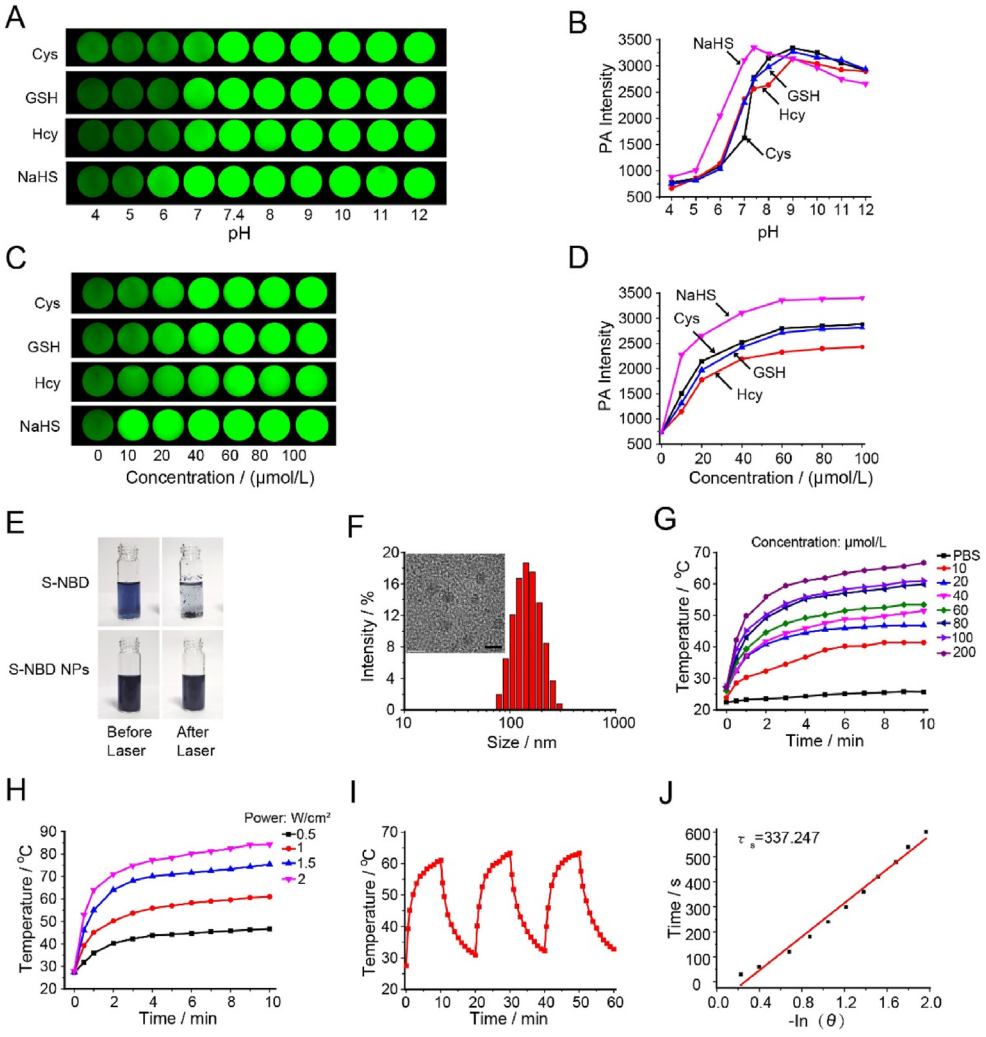

Figure 4 Photoacoustic and photothermal images of S-NBD in solution. (A) PA images of S-NBD (10 μmol/L) reacted with Cys/Hcy/GSH and NaHS in different pH solutions. (B) Quantification of PA signal intensity in (A). (C) PA images of S-NBD reacted with different concentrations of Cys/Hcy/GSH and NaHS (0, 10, 20, 40, 60, 80 and 100 μmol/L) in EtOH/PBS (pH 7.4, *v*/*v*, 5/5). (D) PA signal intensity of images in (C). (E) Comparison of S-NBD and S-NBD NPs before and after 660 nm laser irradiation. (F) DLS of S-NBD NPs insert TEM of S-NBD NPs (Scale bar = 5 nm). (G) The temperature evolution of S-NBD NPs with different concentrations under 660 nm laser irradiation (1 W/cm^2, 10 min). (H) Photothermal heating curves of S-NBD NPs (100 μmol/L) irradiated for 10 min using a 660 nm laser at varied power densities (0.5, 1.0, 1.5, and 2.0 W/cm^2). (I) Temperature elevation of S-NBD NPs (100 μmol/L) under three on/off cycles (1.0 W/cm^2). (J) Time constant for heat transfer of S-NBD NPs.

46.8 °C. Furthermore, the relationship between laser power and temperature changes was assessed for its impact on S-NBD NPs in PBS (Fig. 4H). It was observed that with an increase in laser power, the temperature of the S-NBD NPs solution rapidly increased, confirming a positive correlation between power and temperature. Further analysis on the photostability of S-NBD NPs was carried out *via* continuous monitoring of S-NBD NPs solution (100 μmol/L) temperature changes under NIR laser irradiation (660 nm, 1.0 W/cm^2, 10 min). The irradiation was then stopped, and the solution was allowed to naturally cool to room temperature. Three heating/cooling cycles were repeated. As shown in Fig. 4I, the temperature changed slightly, indicating the robust stability of S-NBD NPs during laser irradiation.

Next, we conducted photothermal conversion experiments, as shown in Fig. 4J, and ultimately calculated the photothermal conversion efficiency of S-NBD NPs to be ~67.1%. The calculation formula is as Eqs. (1)–(4):

$$\eta = hS(\Delta T_1 - \Delta T_2)/I(1-10^{-A}) \quad (1)$$

$$hS = mc/\tau_s \quad (2)$$

$$t = -\tau_s \mathrm{In}(\theta) \quad (3)$$

$$\theta = (T - T_{surr})/(T_{max} - T_{surr}) \quad (4)$$

where ΔT_1 and ΔT_2 represent the maximum temperature change of the compound and H_2O, respectively; I is the laser power (1 W/cm^2); *A* is the absorbance of compound (100 μmol/L) at 660 nm; m and c are the mass and heat capacity of the solvent, respectively (the

specific heat capacity of water is 4.2 J/g); T is the temperature at time t during the cooling process; T_{max} is the highest temperature reached by the compound; T_{surr} is the ambient temperature.

The value of photothermal conversion efficiency indicates better performance than most previously reported photothermal reagents of the same type, including porphyrin (62.5%)[53], cyanine dyes (26.6%)[54], IR820@F-127 NPs (35.2%)[55], IT-TQF NPs (47%)[56] and TCT-NPs (40.1%)[57]. These results confirm the potential of S-NBD NPs as a promising candidate for PTT.

2.4. *Fluorescence/photoacoustic and photothermal imaging in living cells*

Prior to cell imaging, we conducted CCK-8 assays to assess the cytotoxicity of the S-NBD probe in HeLa cells. As depicted in Supporting Information Fig. S34, even where the concentrations of S-NBD and S-NBD NPs were 80 μmol/L, the cell survival rate remains above 90%, highlighting the excellent biocompatibility of S-NBD and S-NBD NPs.

We then investigated the possibility of utilizing S-NBD for imaging endogenous biothiols in tumor cells. It was observed that as S-NBD concentration increased, the fluorescence intensity gradually increased at different channels simultaneously, indicating that S-NBD can effectively detect biothiols in tumor cells (Fig. 5A). The effect of S-NBD incubation time on fluorescence intensity was then verified (Supporting Information Fig. S35), and the results showed that fluorescence intensity reached its peak at the S-NBD concentration of 10 μmol/L and the incubation time of 1 h.

An additional control experiment was devised to verify the capability of S-NBD to respond selectively to Cys/Hcy and GSH *in vivo*, in which the cells were pre-treated with thiol eliminator (*N*-ethylmaleimide, NEM) before the addition of S-NBD. The results indicated significant reductions in fluorescence for both channels. The ability of S-NBD to distinguish and detect biothiols was further explored by pre-incubating cells with NEM (30 μmol/L) for 30 min and then incubating them with S-NBD (10 μmol/L) for 1 h, after which, either Cys/Hcy or GSH (200 μmol/L) were added. The findings indicated that the addition of Cys/Hcy enhanced the red and green fluorescence, while the addition of GSH only enhanced the red fluorescence (Fig. 5B). This result is consistent with the solution-level fluorescence detection results, indicating that the S-NBD probe can detect and distinguish Cys/Hcy from GSH in living cells.

Having verified S-NBD's value for conducting photoacoustic imaging *in vitro*, we sought to investigate its PA imaging performance on cells. It was observed that as the concentration of S-NBD increased, the PA signal at 680 nm gradually increased as

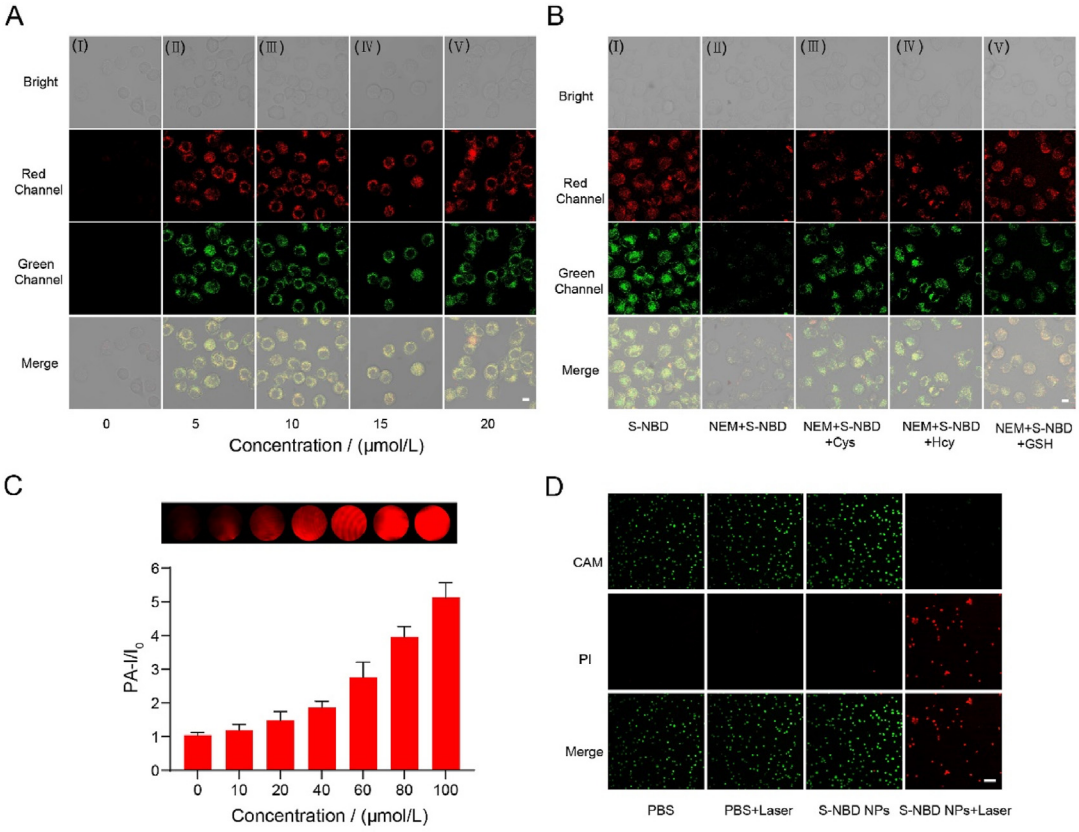

Figure 5 Fluorescence/photoacoustic and photothermal images of cells. (A) (I–V) Fluorescence images of HeLa cells incubated with S-NBD at different concentrations (0, 5, 10, 15, and 20 μmol/L) for 1 h. (B). (I) Cells treated with S-NBD (10 μmol/L). (II) The cells were pre-incubated with NEM (30 μmol/L) for 30 min and then co-incubated with S-NBD (10 μmol/L). The cells were pre-incubated with NEM (30 μmol/L) and then treated with S-NBD (10 μmol/L) for 1 h. Finally, cells were incubated with (III) Cys, (IV) Hcy, and (V) GSH (200 μmol/L). Scale bar = 10 μm. (C) PA images and intensities of HeLa cells incubated with different concentrations of S-NBD (0, 10, 20, 40, 80, and 100 μmol/L) for 1 h. (D) Fluorescence imaging of HeLa cells after different treatments; all cells were stained with calcein-AM and PI. Scale bar = 100 μm.

well (Fig. 5C), suggesting the potentially valuable role of S-NBD for *in vivo* PA imaging.

Furthermore, we assessed the photothermal performance of S-NBD NPs in HeLa cells. Firstly, we quantitatively verified the phototoxicity of the S-NBD probe using a CCK-8 assay and found that when the cells were laser-irradiated at 660 nm, the cell survival rate gradually decreased with an increase in the probe concentration. When the concentration reached 80 μmol/L, the cell survival rate was approximately 15% (Supporting Information Fig. S36). These results indicated the lower dark toxicity and higher phototoxicity of the cells. The cells were then stained with calcein-AM (which produces green fluorescence in living cells) and propidium iodide (which produces red fluorescence in dead cells) to visually confirm the phototoxicity of the probe. As shown in Fig. 5D, both PBS groups (with or without laser) and the S-NBD NPs without laser group exhibited strong green fluorescence, while the S-NBD NPs + laser group showed strong red fluorescence and weak green fluorescence, indicating a higher number of dead cells. This outcome further attests to the impressive photothermal performance of S-NBD NPs.

2.5. *Fluorescence/photoacoustic imaging biothiols in tumor-bearing mice*

In light of the S-NBD probe's promising NIRF and PA performance on biothiols *in vitro*, we extended our investigation to evaluate the imaging efficacy of S-NBD in tumor-bearing mice. To this end, a HeLa-xenograft tumor mice model was established to assess the *in vivo* fluorescence and photoacoustic imaging capabilities of S-NBD. The *in vivo* fluorescence images of the mice, captured after S-NBD administration, are depicted in Fig. 6A and B. It was observed that S-NBD was localized at the tumor site, producing fluorescence and PA enhancement. Experiments have shown that S-NBD is highly responsive to tumor cells where biothiols are overexpressed. As time elapsed post-injection, the fluorescence/PA intensity at the tumor site in the S-NBD group progressively increased, peaking at 4 h before diminishing, as illustrated in Fig. 6C and D.

We then administered S-NBD (500 μmol/L, 100 μL) *via* injection to two groups of mice, with the only difference being that one group had been injected with NEM 30 min in advance. After

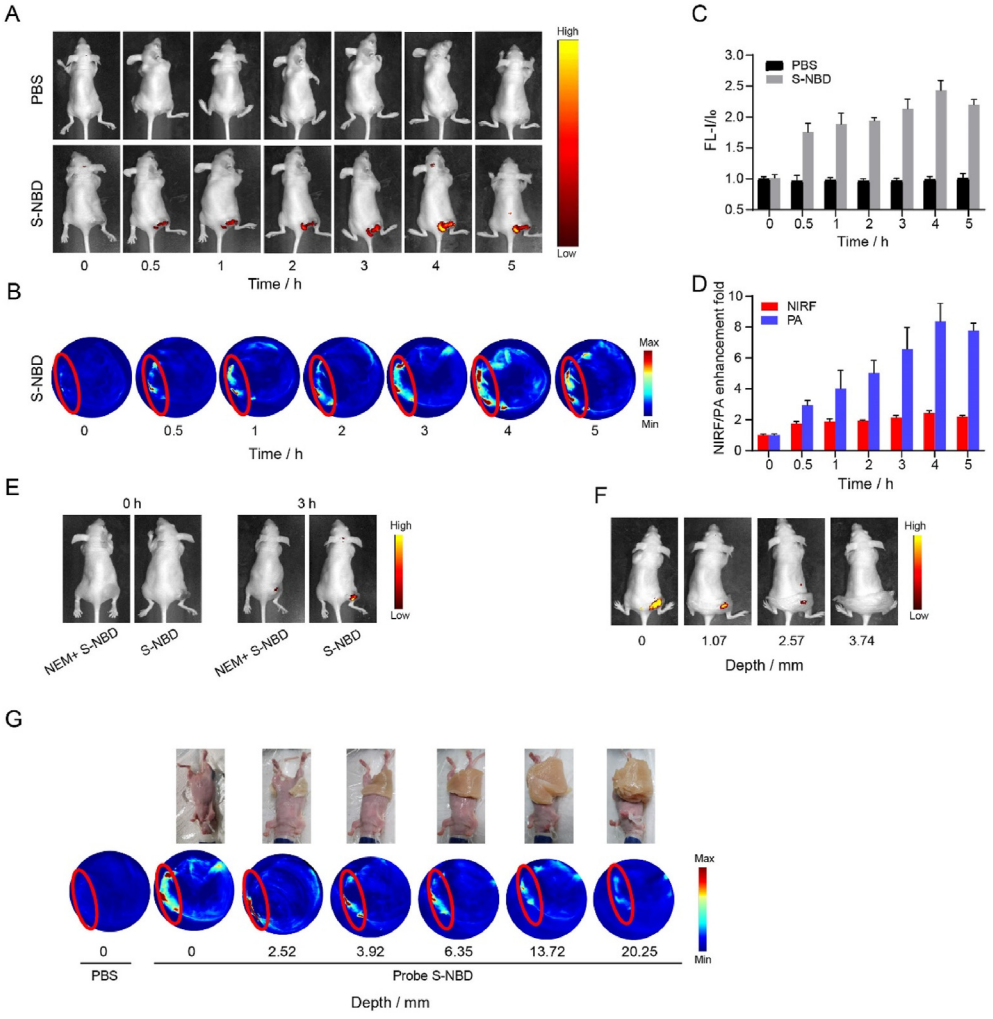

Figure 6 Dual-mode imaging of tumor-bearing mice. (A) From left to right, after injecting PBS and S-NBD into the tumor, the images were obtained at 0, 0.5, 1, 2, 3, 4, and 5 h. (B) The time-dependent PA imaging of tumor-bearing mice. (C) Quantitative analysis of fluorescence intensity of images in (A). (D) Quantitative analysis of NIRF/PA enhancement multiples in (A) and (B). (E) NIRF images of mice injected with NEM + S-NBD and S-NBD only. (F) The NIRF images of the tumor site of mice were covered with chicken flesh of different thicknesses. (G) PA images of mice covered with chicken flesh of different thicknesses.

3 h, we observed that the fluorescence signal at the tumor site in mice injected with NEM was weaker than that in the mice that did not receive NEM. This finding indicates that S-NBD can sensitively detect changes in the concentration of biothiols *in vivo* (Fig. 6E). Subsequently, when the S-NBD probe was used to detect biothiols, the tumor site was covered with chicken flesh of varying thicknesses to analyze the probe's ability to penetrate tissue during NIRF/PA imaging. As expected, the increases in the thickness of the chicken flesh led to decreases in the strength of the fluorescence signal. When the thickness reached 3.74 mm, the fluorescence signal almost disappeared completely (Fig. 6F). Similarly, PA images of the mice were obtained when they were covered with chicken flesh of different thicknesses, revealing that the PA signal likewise decreased as thickness increased (Fig. 6G). When the penetration depth reached 20.25 mm, the PA signal at the tumor site virtually disappeared. These results indicate that photoacoustic imaging possesses better tissue penetration ability and can detect overexpressed biothiols in deep tissues.

2.6. *Photothermal therapy in tumor-bearing mice*

The S-NBD probe displayed exemplary photothermal performance at both the solution and cellular levels. We therefore decided to test the PTT capabilities of S-NBD NPs in tumor-bearing mice, as shown in Fig. 7A. The temperature changes at the tumor sites in mice from the PBS + laser and S-NBD NPs + laser groups are depicted in Fig. 7B−C. It can be observed that the temperature at the tumor sites of mice in the PBS + laser group increased from 30.2 to 38.4 °C, demonstrating a weak PTT effect. Conversely, the temperature in the S-NBD NPs + laser group rose rapidly from 30.2 to 60.8 °C. This marked increase was significantly higher than that observed in the PBS group and exceeds the threshold for tumor thermal ablation, demonstrating the potential for effective PTT. Post-PTT, the body weights and tumor volumes of the mice in each group were measured daily, as shown in Fig. 7D−F.

All four groups exhibited no significant changes in body weight, further indicating S-NBD NPs' biocompatibility. The tumors in the PBS group, PBS + laser group, and S-NBD NPs group were found to gradually increase, suggesting that laser irradiation and S-NBD NPs alone have little effect on tumor growth. Only in the S-NBD NPs +660 nm laser irradiation group was significant tumor inhibition observed, indicating a robust PTT effect. On the thirteenth day, the mice in each group were dissected, and tumor samples were examined, revealing the complete elimination of tumors in the S-NBD NPs + laser group (Fig. 7G).

Moreover, we examined the potential toxicity of PTT to other vital organs. An evaluation of major organs (heart, liver, spleen, lungs, and kidneys) in all four groups of mice was conducted through hematoxylin and eosin (H&E) staining (Fig. 7H). These results did not show significant physiological and morphological changes in any of these organs, corroborating the safety of S-NBD NPs in PTT.

3. Conclusions

This study introduces a novel multifunctional probe, S-NBD, designed for the dual purpose of detecting biothiols and facilitating photothermal therapy for tumors. Upon reacting with biothiols, the probe exhibits near-infrared fluorescence at 838 nm, accompanied by NRFI and PA signals, enabling sensitive deep tissue detection of biothiols. The introduction of the NBD structure further allows for the differentiation of Cys/Hcy from GSH/NaHS. At the same time, the probe demonstrates excellent photothermal performance. Based on the D−π−A mechanism, the diphenylamine structure was introduced into the core skeleton of dicyanoisophorone-xanthene, forming a structure similar to triphenylamine and endowing it with photothermal properties. The encapsulation of S-NBD into an amphiphilic copolymer F-127 yielded S-NBD NPs with excellent photostability, high photothermal conversion efficiency (67.1%), and good biocompatibility. S-NBD, administered locally, can induce heating at tumor sites and achieve the effect of tumor thermal ablation. This study described the development of a pioneering probe capable of multimodal biothiol detection and simultaneous photothermal therapy, offering a new tool for the comprehensive diagnosis and treatment of tumors and cervical cancer.

4. Experimental

4.1. *Materials and instruments*

Detailed information regarding the materials and equipment employed in this study can be found in Supporting Information.

4.2. *Fluorescent detection for biothiols in vitro*

A stock solution of S-NBD (1 mmol/L) was prepared in DMSO. The probe stock solution was added to EtOH/PBS buffer (pH 7.4, *v*/*v*, 5/5) to achieve a 10 μmol/L S-NBD solution. Subsequently, different concentrations of biothiols were introduced, and the fluorescence emission spectra were recorded as follows: λ_{ex} = 470 nm, λ_{em} = 490−700 nm and λ_{ex} = 660 nm, λ_{em} = 750−1000 nm.

4.3. *The density functional theory calculations*

Gaussian 09 software was employed to carry out theoretical calculations. The ground-state structures of probes S-NBD and S−OH were optimized using density functional theory (DFT) combined with the B3LYP functional[47-49] and the 6-31+G (d, p) basis set[50]. The SMD implicit solvent model, with ethanol as the solvent, was applied to calculate the optimal geometric structure and electronic transitions of the probe. The resultant data were analyzed using Multiwfn 3.7 software[51,52] and rendered using the VMD 1.9.3 program[52]. The fluorescence spectra of the designed molecules were calculated from the optimized structure using the TD-B3LYP/6-31G (d, p) basis set.

4.4. *Photoacoustic imaging for biothiols in vitro*

For photoacoustic imaging, various concentrations of biothiols were added to 1.5 mL EtOH/PBS buffer (pH 7.4, *v*/*v*, 5/5) containing 10 μmol/L S-NBD solution. Subsequently, the centrifuge tube was placed in the photoacoustic device for photoacoustic imaging (λ_{ex} = 680 nm).

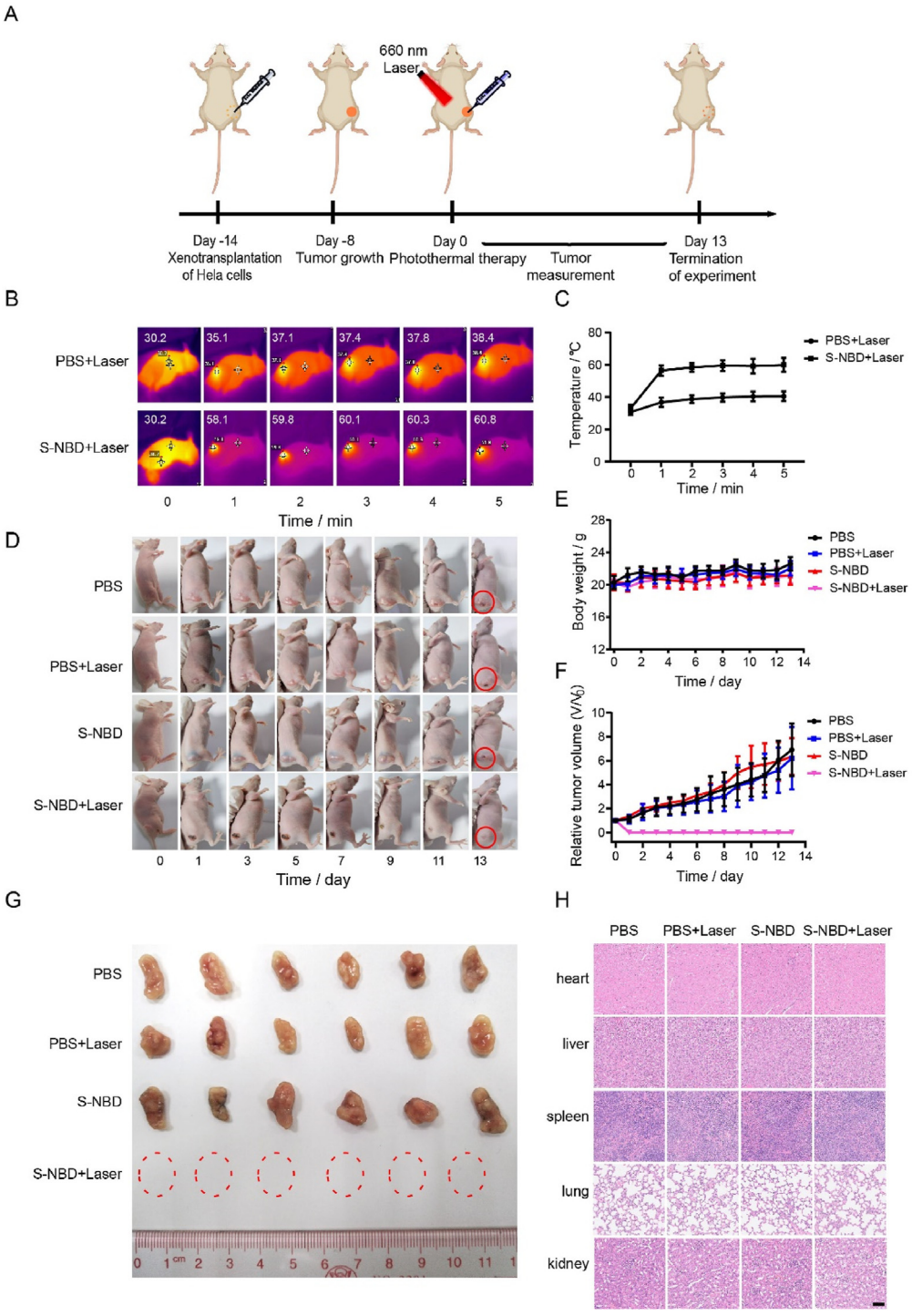

Figure 7 Photothermal therapy in tumor-bearing mice. (A) Schematic illustration of animal experiment process. (B) Photothermal images of tumor-bearing mice in the PBS group and S-NBD NP group, irradiated by 660 nm laser for 5 min. (C) The temperature change curve of the tumor area in (B). (D) Photographs of the tumor-bearing mice in PBS, PBS + laser group, S-NBD NPs, and S-NBD NPs + laser group at Days 0, 1, 3, 5, 7, 9, 11, and 13. (E) The body weight change diagram in the above groups. (F) The tumor growth curves in the above groups. (G) The tumor maps of the tumor-bearing mice in the above groups were dissected on the 13th day. (H) H&E staining images of heart, liver, spleen, lung, and kidney tissues of tumor-bearing mice in the above groups. Scale bar = 50 μm.

4.5. Photothermal imaging for biothiols in vitro

For photothermal imaging, S-NBD NPs of different concentrations were placed in a small transparent glass bottle and then irradiated with a 660 nm laser. During the irradiation process, an infrared thermal camera (FLUKE-VT08/CN, Fluke Instruments (Shanghai) Co., Ltd.) was used to capture photothermal images and record real-time temperature.

4.6. Fluorescence/photoacoustic imaging in living cells

For biothiol fluorescence/photoacoustic imaging in living cells, cells were incubated with different concentrations of S-NBD for 1 h before fluorescence/photoacoustic imaging.

4.7. Fluorescence/photoacoustic imaging in tumor-bearing mice

Six-week-old female BALB/C nude mice were used for animal experiments. The tumor model was established through the subcutaneous injection of 2×10^6 HeLa cells (in PBS) into the mice. The Hale-xenograft tumor mice were divided into two groups for separate treatment. One group was injected with 100 μL PBS, and the other group was injected with 100 μL PBS containing 500 μmol/L S-NBD. The probe S-NBD has poor water solubility, so we added 5% solvent Solutol HS-15 to aid in the *in vivo* fluorescence/photoacoustic imaging of tumor bearing mice. All of the above injection methods consisted of intratumoral injections. There are two reasons for using intratumoral injection instead of other injection methods: firstly, the probe S-NBD has poor water solubility, and tail vein injection can easily block blood vessels; Secondly, tail vein injection with nanoparticles is used. Due to the EPR effect, S-NBD NPs solution will accumulate at the tumor site and produce fluorescence, but the imaging effect is not as good as intratumoral injection. Mice were then positioned in the imaging chamber and subjected to imaging using the small animal optical *in vivo* imaging system. For photoacoustic imaging, the mice were anesthetized with isoflurane and remained anesthetized throughout the imaging process (λ_{ex} = 680 nm).

4.8. Photothermal therapy in tumor-bearing mice

When the tumor size of the HeLa tumor-bearing mice reached 80−120 mm^3, the mice were randomly divided into four groups: PBS control group (50 μL), PBS + 660 nm laser irradiation group (1.0 W/cm^2, 5 min), S-NBD NPs (300 μmol/L, 50 μL) treated group, and S-NBD NPs + 660 nm laser irradiation group. All the above injection methods consisted of intratumoral injections. The two groups requiring laser treatment were irradiated with a 660 nm laser for 5 min after injection of PBS and the S-NBD probe. During this process, the temperature was monitored and photographed using an IR thermal camera.

Acknowledgments

This study was supported by Foundation of Ministry of Science and Technology of China (2022YFC2304203), National Natural Science Foundation of China (Nos. 82073689, 82273762 and 81973183), National Natural Science Foundation of Guangdong Province (No. 2024A1515010642, China) and Science and Technology Program of Guangzhou (No. 201904010380, China).

Author contributions

Liu Shi: Writing − original draft. Zhenzhou Chen: Methodology. Jiaxin Ou: Methodology. Lan Huang: Writing − review & editing. Kui Cheng: Supervision.

Conflicts of interest

The authors declare no conflicts of interest.

Appendix A. Supporting information

Supporting information to this article can be found online at https://doi.org/10.1016/j.apsb.2024.07.017.

References

1. Tan X, Ji K, Wang X, Yao R, Han G, Villamena FA, et al. Discriminative detection of biothiols by electron paramagnetic resonance spectroscopy using a methanethiosulfonate trityl probe. *Angew Chem* 2020;**59**:928−34.
2. Nagendraraj T, Priya SV, Annaraj J, Sagadevan S. Targeted cysteine and glutathione detection in extra/intracellular systems by copper-based fluorescent imaging probes. *Coord Chem Rev* 2023;**495**:215368.
3. Mishanina TV, Libiad M, Banerjee R. Biogenesis of reactive sulfur species for signaling by hydrogen sulfide oxidation pathways. *Nat Chem Biol* 2015;**11**:457−64.
4. Cao T, Xu T, Xu R, Shu X, Liao S. Decarboxylative thiolation of redox-active esters to free thiols and further diversification. *Nat Commun* 2020;**11**:5340.
5. Zhang S, Ong C, Shen H. Critical roles of intracellular thiols and calcium in parthenolide-induced apoptosis in human colorectal cancer cells. *Cancer Lett* 2004;**208**:143−53.
6. Yang Y, Zhou K, Ma M, Liu H, Jin M, Yin C, et al. Thiol "click" chromene mediated cascade reaction forming coumarin for *in-situ* imaging of thiol flux in drug-induced liver injury. *Chem Eng J* 2023;**452**:139020.
7. Jouandin P, Marelja Z, Shih Y, Parkhitko AA, Dambowsky M, Asara JM, et al. Lysosomal cystine mobilization shapes the response of torc1 and tissue growth to fasting. *Science* 2022;**375**:eabc4203375.
8. Hermann A, Sitdikova G. Homocysteine: biochemistry, molecular biology and role in disease. *Biomolecules* 2021;**11**:737.
9. Desideri E, Ciccarone F, Ciriolo MR. Targeting glutathione metabolism: partner in crime in anticancer therapy. *Nutrients* 2019;**11**:1926.
10. Wu X, Sun X, Guo Z, Tang J, Shen Y, James TD, et al. *In vivo* and *in situ* trac-king cancer chemotherapy by highly photostable NIR fluorescent theranostic prodrug. *J Am Chem Soc* 2014;**136**:3579−88.
11. Kolluru GK, Shackelford RE, Shen X, Dominic P, Kevil CG. Sulfide regulation of cardiovascular function in health and disease. *Nat Rev Cardiol* 2023;**20**:109−25.
12. Dilek N, Papapetropoulos A, Toliver-Kinsky T, Szabo C. Hydrogen sulfide: an endogenous regulator of the immune system. *Pharmacol Res* 2020;**161**:105119.
13. Zou X, Zhao Y, Lin W. Photoacoustic/fluorescence dual-modality cyanine-based probe for real-time imaging of endogenous cysteine and in situ diagnosis of cervical cancer *in vivo*. *Anal Chim Acta* 2023;**1239**:340713.
14. Liu H, Chen L, Xu C, Li Z, Zhang H, Zhang X, et al. Recent progresses in small-molecule enzymatic fluorescent probes for cancer imaging. *Chem Soc Rev* 2018;**47**:7140−80.
15. Hou J, Ren WX, Li K, Seo J, Sharma A, Yu X, et al. Fluorescent bioimaging of pH: from design to applications. *Chem Soc Rev* 2017;**46**:2076−90.
16. Yuan L, Lin W, Zheng K, He L, Huang W. Far-red to near infrared analyte-responsive fluorescent probes based on organic fluorophore platforms for fluorescence imaging. *Chem Soc Rev* 2013;**42**:622−61.
17. Guo Z, Park S, Yoon J, Shin I. Recent progress in the development of near-infrared fluorescent probes for bioimaging applications. *Chem Soc Rev* 2014;**43**:16−29.
18. Niu L, Chen Y, Zheng H, Wu L, Tung C, Yang Q. Design strategies of fluorescent probes for selective detection among biothiols. *Chem Soc Rev* 2015;**44**:6143−60.
19. Ntziachristos V, Razansky D. Molecular imaging by means of multispectral optoacoustic tomography (msot). *Chem Rev* 2010;**110**:2783−94.

20. Gujrati V, Mishra A, Ntziachristos V. Molecular imaging probes for multi-spectral optoacoustic tomography. *Chem Commun* 2017;**53**:4653−72.
21. Huang X, Song J, Yung BC, Huang X, Xiong Y, Chen X. Ratiometric optical nanoprobes enable accurate molecular detection and imaging. *Chem Soc Rev* 2018;**47**:2873−920.
22. Ding W, Yao S, Chen Y, Wu Y, Li Y, He W, et al. A near-infrared fluorescent and photoacoustic probe for visualizing biothiols dynamics in tumor and liver. *Molecules* 2023;**28**:2229.
23. Tian Y, Jiang W, Wang W, Mao G, Li Y, Li C. NHD(P)H-triggered probe for dual-modal imaging during energy metabolism and novel strategy of enhanced photothermal therapy in tumor. *Biomaterials* 2021;**271**:120736.
24. Zhang L, Zhuang W, Yuan Y, Shen J, Shi W, Liu G, et al. Novel glutathione activated smart probe for photoacoustic imaging, photothermal therapy, and safe postsurgery treatment. *ACS Appl Mater Inter* 2022;**14**:24174−86.
25. Mondal S, Montaño-Priede JL, Nguyen VT, Park S, Choi J, Doan VHM, et al. Computational analysis of drug free silver triangular nanoprism theranostic probe plasmonic behavior for *in-situ* tumor imaging and photothermal therapy. *J Adv Res* 2022;**41**:23−38.
26. Kong X, Wan G, Li B, Wu L. Recent advances of polyoxometalates in multi-functional imaging and photothermal therapy. *J Mater Chem B* 2020;**8**:8189−206.
27. Zhang X, Xuan Y, Yang X, Cheng K, Zhang R, Li C, et al. A multifunctional targeting probe with dual-mode imaging and photothermal therapy used *in vivo*. *J Nanobiotechnology* 2018;**16**:42.
28. Liu Y, Mo F, Hu J, Jiang Q, Wang X, Zou Z, et al. Precision photothermal therapy and photoacoustic imaging by *in situ* activatable thermoplasmonics. *Chem Sci* 2021;**12**:10097−105. Cambridge.
29. Zhi D, Yang T, O'Hagan J, Zhang S, Donnelly RF. Photothermal therapy. *J Control Release* 2020;**325**:52−71.
30. Kennedy LC, Bickford LR, Lewinski NA, Coughlin AJ, Hu Y, Day ES, et al. A new era for cancer treatment: gold-nanoparticle-mediated thermal therapies. *Small* 2011;**7**:169−83.
31. Qi K, Sun B, Liu S, Zhang M. Research progress on carbon materials in tumor photothermal therapy. *Biomed Pharmacother* 2023;**165**:115070.
32. Hou Y, Zhang P, Wang D, Liu J, Rao W. Liquid metal hybrid platform-mediated ice-fire dual noninvasive conformable melanoma therapy. *ACS Appl Mater Inter* 2020;**12**:27984−93.
33. Wang B, Chen Z, Cen X, Liang Y, Tan L, Liang E, et al. A highly selective and sensitive chemiluminescent probe for leucine aminopeptidase detection *in vitro, in vivo* and in human liver cancer tissue. *Chem Sci* 2022;**13**:2324−30.
34. Yang J, Pan Y, Zeng X, Liu S, Chen Z, Cheng K. Discovery of novel aporphine alkaloid derivative as potent tlr2 antagonist reversing macrophage polarization and neutrophil infiltration against acute inflammation. *Acta Pharm Sin B* 2023;**13**:3782−801.
35. Cen X, Wang B, Liang Y, Chen Y, Xiao Y, Du S, et al. Small molecule smu-cx24 targeting toll-like receptor 3 counteracts inflammation: a novel approach to atherosclerosis therapy. *Acta Pharm Sin B* 2022;**12**:3667−81.
36. Chen Y, Zhi S, Ou J, Gao J, Zheng L, Huang M, et al. Cancer cell membrane-coated nanoparticle co-loaded with photosensitizer and toll-like receptor 7 agonist for the enhancement of combined tumor immunotherapy. *ACS Nano* 2023;**17**:16620−32.
37. Wu Y, Yang Z, Cheng K, Bi H, Chen J. Small molecule-based immunomodulators for cancer therapy. *Acta Pharm Sin B* 2022;**12**:4287−308.
38. Chen Z, Wang B, Liang Y, Shi L, Cen X, Zheng L, et al. Near-infrared fluorescent and photoacoustic dual-mode probe for highly sensitive and selective imaging of cysteine *in vivo*. *Anal Chem* 2022;**94**:10737−44.
39. Liu J, Wang Z, Mao G, Jiang W, Tan M, Xu F, et al. A near-infrared fluorescent probe with large Stokes shift for imaging cys in tumor mice. *Anal Chim Acta* 2021;**1171**:338655.
40. Zhang D, Yang J, Ye S, Wang Y, Liu C, Zhang Q, et al. Combination of photothermal therapy with anti-inflammation therapy attenuates the inflammation tumor microenvironment and weakens immunosuppression for enhancement antitumor treatment. *Small* 2022;**18**:e2107071.
41. Zhang Y, Wang J, Wang S, Zhu X, Yu Z, Wu Z, et al. Simultaneous one-step regulation of planarization and donor rotation to enhance multi-modal imaging guided therapy. *Mater Chem Front* 2022;**6**:2921−8.
42. Zhang Z, Xu W, Kang M, Wen H, Guo H, Zhang P, et al. An all-round athlete on the track of phototheranostics: subtly regulating the balance between radiative and nonradiative decays for multimodal imaging-guided synergistic therapy. *Adv Mater* 2020;**32**:e2003210.
43. Yang Z, Zhang Z, Lei Z, Wang D, Ma H, Tang BZ. Precise molecular engineering of small organic phototheranostic agents toward multimodal imaging-guided synergistic therapy. *ACS Nano* 2021;**15**:7328−39.
44. Zhang Y, Ni Y, Zhao X, Wang T, Zhu X, Sun X, et al. Tumor stimulus-activatable pretheranostic agent: one key to three locks. *Anal Chem* 2023;**95**:15636−44.
45. Tian Y, Zhou D, Jiang W, She Z, Li Y, Li C. Novel near-infrared fluorescence probe with large stokes shift for monitoring ccl4-induced toxic hepatitis. *Talanta* 2021;**223**:121720.
46. Yang Z, Mo Q, He J, Mo D, Li J, Chen H, et al. Mitochondrial-targeted and near-infrared fluorescence probe for bioimaging and evaluating monoamine oxidase a activity in hepatic fibrosis. *ACS Sens* 2020;**5**:943−51.
47. Becke Axel D. Density-functional thermochemistry. III. The role of exact exchange. *J Chem Phys* 1993;**98**:5648−52.
48. Stephens PJ, Devlin FJ, Chabalowski CF, Frisch MJ. Ab initio calculation of vibrational absorption and circular dichroism spectra using density functional force fields. *J Phys Chem* 1994;**98**:11623−7.
49. Yang W, Parr RG, Lee C. Development of the colle-salvetti correlation-energy formula into a functional of the electron density. *Phys Rev B* 1988;**37**:785−9.
50. Rassolov VA, Ratner MA, Pople JA, Redfern PC, Curtiss LA. 6-31g* basis set for third-row atoms. *J Comput Chem* 2001;**22**:976−84.
51. Lu T, Chen F. Multiwfn: a multifunctional wavefunction analyzer. *J Comput Chem* 2012;**33**:580−92.
52. Humphrey WF, Dalke A, Schulten K. VMD: visual molecular dynamics. *J Mol Graph* 1996;**14**:33−8.
53. Wu F, Chen L, Yue L, Wang K, Cheng K, Chen J, et al. Small-molecule porphyrin-based organic nanoparticles with remarkable photothermal conversion efficiency for *in vivo* photoacoustic imaging and photothermal therapy. *ACS Appl Mater Inter* 2019;**11**:21408−16.
54. Li S, Sun Z, Deng G, Meng X, Li W, Ni D, et al. Dual-modal imaging-guided highly efficient photothermal therapy using heptamethine cyanine-conjugated hyaluronic acid micelles. *Biomater Sci* 2017;**5**:1122−9.
55. Fan H, Chen S, Du Z, Yan T, Alimu G, Zhu L, et al. New indocyanine green therapeutic fluorescence nanoprobes assisted high-efficient photothermal therapy for cervical cancer. *Dyes Pigm* 2022;**200**:110174.
56. Lou H, Ji A, Qu C, Liu H, Jiang L, Chen H, et al. A small-molecule based organic nanoparticle for photothermal therapy and near-infrared-IIb imaging. *ACS Appl Mater Inter* 2022;**14**:35454−65.
57. Gao J, Yuan L, Min Y, Yu B, Cong H, Shen Y. D-A-D organic fluorescent probes for NIR-II fluorescence imaging and efficient photothermal therapy of breast cancer. *Biomater Sci* 2024;**12**:1320−31.